

Microscopic mechanism of the noncrystalline anisotropic magnetoresistance in (Ga,Mn)AsKarel Výborný,¹ Jan Kučera,¹ Jairo Sinova,^{2,1} A. W. Rushforth,³ B. L. Gallagher,³ and T. Jungwirth^{1,3}¹*Institute of Physics, ASCR, v. v. i., Cukrovarnická 10, CZ-16253 Praha 6, Czech Republic*²*Department of Physics, Texas A&M University, College Station, Texas 77843-4242, USA*³*School of Physics and Astronomy, University of Nottingham, Nottingham NG7 2RD, United Kingdom*

(Received 25 April 2009; revised manuscript received 7 September 2009; published 9 October 2009)

Starting with a microscopic model based on the Kohn-Luttinger Hamiltonian and kinetic p - d exchange combined with Boltzmann formula for conductivity we identify the scattering from magnetic Mn combined with the strong spin-orbit interaction of the GaAs valence band as the dominant mechanism of the anisotropic magnetoresistance (AMR) in (Ga,Mn)As. This fact allows to construct a simple analytical model of the AMR consisting of two heavy-hole bands whose charge carriers are scattered on the impurity potential of the Mn atoms. The model predicts the correct sign of the AMR (resistivity parallel to magnetization is smaller than perpendicular to magnetization) and identifies its origin arising from the destructive interference between electric and magnetic part of the scattering potential of magnetic ionized Mn acceptors when the carriers move parallel to the magnetization.

DOI: [10.1103/PhysRevB.80.165204](https://doi.org/10.1103/PhysRevB.80.165204)

PACS number(s): 71.70.Ej, 72.25.Rb, 75.47.-m

I. INTRODUCTION

Although it has been known for 150 years that electric resistance of a magnetic metal depends on the direction of magnetization,¹ the origin of such dependence is often explained only vaguely as an interplay of spin-orbit interaction (SOI) and magnetization. Conceptual questions around this phenomenon, the anisotropic magnetoresistance (AMR), remain open and relate to the quest for its detailed mechanism, its sign and specific magnitude. Our ability to control the AMR by material design, with potential impact on new electronic devices,² would be improved if we had answers more specific but nevertheless still more universal than “black-box-like” modeling of AMR in each and every deamable system.

Several factors obstruct a clearer insight into the phenomenon: there are many electronic bands crossing the Fermi level in most materials and the AMR of a crystalline material has various contributions of different symmetries. *Ab initio* calculations performed in FeNi (Ref. 3) and FeCo (Ref. 4) disordered alloys agree reasonably well with experimentally determined AMR but they do not allow for any detailed conclusions about its mechanisms. On the other hand, the

model⁵ of current-carrying s -states scattered to spin-orbit-coupled d -states provides a relatively transparent picture of the AMR (Ref. 6) but requires the fitting of one or more phenomenological parameters and even then a clear-cut correspondence to *ab initio* results for ferromagnetic transition metals could not be established.³

Diluted magnetic semiconductors, and (Ga,Mn)As in particular, offer a promising system in which these issues become simplified:⁷ Fermi level lies close to the top of the valence band so that $\mathbf{k}\cdot\mathbf{p}$ approximation can be used, few bands are involved in transport, and in addition, their SOI is strong. Moreover, experiments done so far show that the noncrystalline component of the AMR,^{8,9} arising from the breaking of the symmetry by choosing a specific current direction, outweighs the crystalline components in most of the metallic highly Mn-doped materials. In attempting to describe the AMR in such system, we can begin with a model isotropic but still spin-orbit coupled band structure and add the effect of magnetization in the three possible distinct ways, as sketched in Fig. 1. Either (a) the magnetization induces a magnetotransport anisotropy via the SOI already at the level of group velocities of the exchange-split Fermi surfaces,¹⁰ (b) it may enter via anisotropic scattering of the

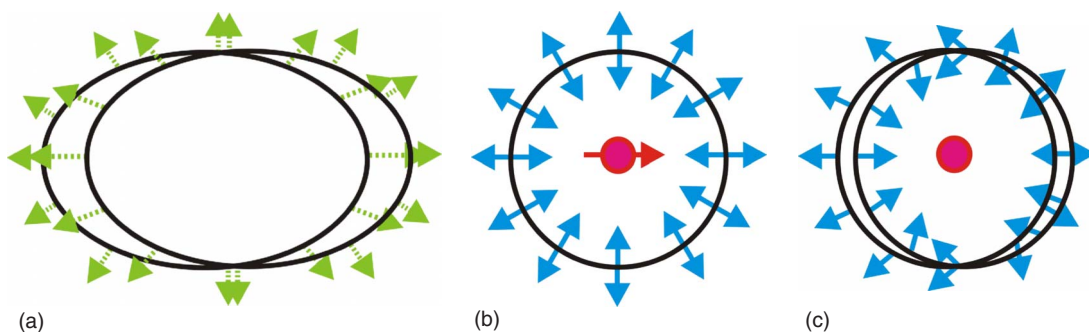


FIG. 1. (Color online) The AMR can originate from three distinct mechanisms combining magnetization (pointing to the right and coupled antiferromagnetically to charge carrier spins in this sketch) and SOI, that break the isotropy: (a) anisotropic Fermi velocities (arrows) along the Fermi surface for the charge carriers, or anisotropic relaxation rates due to (b) unpolarized bands (represented by the indicated isotropic spin texture) scattered by anisotropic impurities or (c) partially polarized bands scattered by isotropic impurities.

unpolarized spin-orbit coupled carriers from polarized magnetic impurities, or (c) via anisotropic scattering of partially polarized carriers which does not require a magnetic character of the scatterers. Transport calculations must of course always include an account of scattering but it is its anisotropy that is disregarded within mechanism (a); in mechanisms (b) and (c) it is in turn the anisotropy of the group velocities that is neglected (a more detailed discussion is presented in Sec. II C). We point out that the mechanisms (a) and (c) represent a situation where both fundamental ingredients of the AMR (SOI and magnetization) are present in the same states of the band structure. The SOI is necessary for AMR to occur but, at the same time, it weakens the effect of magnetization so that weaker AMR may be expected whenever the mechanisms (a) or (c) dominate. On the other hand, in mechanism (b), the SOI in an unpolarized carrier band can be strong while the magnetization of the impurities remains at 100%. Consequently, very large AMR can arise if this mechanism is important.¹¹

We show in this paper that metallic (Ga,Mn)As is a favorable system for the purposes of studying AMR. Not only because of its relatively simple (effective) Hamiltonian (described in Sec. II) and the dominance of the AMR mechanism (b), but also because of the way the AMR model can be simplified (as shown in Sec. III) down to analytical formulae revealing the basic AMR trends (see Sec. IV). This analysis is our main result together with the detailed explanation of the AMR sign in (Ga,Mn)As (resistance parallel to magnetization is smaller than perpendicular to magnetization) which is observed experimentally^{8,9,12–18} and is opposite to most magnetic metals.^{19,20} The results in Sec. IV include analytically evaluated anisotropic conductivity on several levels of model complexity, and the most simplified model allows to clearly identify the physical mechanism that determines the sign of the AMR in (Ga,Mn)As. Our approach²¹ is based on the relaxation-time approximation (RTA) and it would be desirable to put the present results into more precise terms by exactly solving the Boltzmann equation in its full integral form as the authors did for the simpler Rashba system recently.^{11,22} Although this solution is presently not available, we explain in a short discussion at the end of Sec. IV that the RTA reproduces at least the basic features of the AMR as presented in this work.

II. BASIC MODEL OF AMR IN METALLIC (GA,MN)AS

Three principal ingredients, described in Secs. II A–II C, are necessary to model the conductivity and its magnetic anisotropy: (A) The band structure yielding the spectrum and wave functions, (B) the scattering mechanism, and (C) a transport formalism which combines the former two and produces the conductivity tensor. Given that we base our approach to (C) on relaxation-time approximate solution to the semiclassical Boltzmann equation, we basically need the Fermi velocities derived from the band dispersions, and the relaxation times calculated from the spectrum, wave functions and the relevant form of the impurity potential.

A. Virtual-crystal kinetic-exchange model of (Ga,Mn)As bands

The valence-band kinetic-exchange model of (Ga,Mn)As with metallic conductivities is an established qualitative and

often semiquantitative theoretical approach.^{7,23} The description is based on the canonical Schrieffer-Wolff transformation of the Anderson Hamiltonian²⁴ which for (Ga,Mn)As replaces hybridization of Mn *d* orbitals with As and Ga *sp* orbitals by an effective spin-spin interaction of ($L=0$; $S=5/2$) local moments with host valence-band states. This step proves essential to effectively separate the different AMR mechanisms (a,b,c), symbolized in Fig. 1, because—except for the spin-spin interaction which will be treated as we review below—it completely detaches the Mn states from the spin-orbit coupled host-valence-band states. These valence-band states are conveniently parametrized by the Luttinger parameters $\gamma_1, \gamma_2, \gamma_3$ and spin-orbit splitting Δ_{SO} in the six-band Kohn-Luttinger Hamiltonian^{25–27} H_{KL} . The local interaction between Mn magnetic moments S_I (located at \mathbf{R}_I) and valence hole spins s (at \mathbf{r}), being at the root of the carrier-mediated ferromagnetism in (Ga,Mn)As, is the kinetic exchange and it is described by single parameter^{7,28} J_{pd} . In order to model the band structure of (Ga,Mn)As including disorder electrical potential V associated with the Mn magnetic moments, we treat the Hamiltonian

$$H = H_{KL} + V_{dis} = H_{KL} + J_{pd} \sum_I S_I \cdot s \delta(\mathbf{r} - \mathbf{R}_I) + \sum_I V(\mathbf{r} - \mathbf{R}_I) \quad (1)$$

by the virtual-crystal mean-field²⁶ approximation, whence we get the single-particle Hamiltonian (in momentum representation) of the (Ga,Mn)As valence band

$$H = H_{KL} + h \hat{e}_M \cdot s. \quad (2)$$

Here, \hat{e}_M stands for the unit vector in the direction of the mean-field magnetization, $h = J_{pd} N_{Mn} S_{Mn}$, and the magnetic moment of Mn is $S_{Mn} = 5/2$. In this paper, we will only consider substitutional Mn with volume density N_{Mn} as in optimally annealed samples,²⁹ and assume zero temperature. In the band-structure model, we thus disregard the randomness in the Mn distribution over the crystal and the ensuing spatial inhomogeneity of the exchange interaction, and also we completely ignore the disorder defined by the electrical potential V in Eq. (1) of every single substitutional Mn which is an ionized acceptor. Within this approximation, the effect of the Mn atoms present in the crystal is reduced only to the effective Zeeman-like term in Eq. (2) due to the kinetic exchange of the valence holes with the Mn *d* states. Explicit form of the \mathbf{k} -dependent 6×6 matrix H_{KL} in a convenient basis is given e.g. by Eq. (A8) of the first of Ref. 26.

As we are aiming at a simple model of the noncrystalline AMR component only, we will treat H_{KL} in the spherical approximation, implemented by setting γ_2, γ_3 to their average value.²⁵ In this approximation the dispersion of all six valence bands becomes isotropic in the absence of the kinetic-exchange field. The 6×6 Hamiltonian (2) can be diagonalized numerically and provide the valence bands $E_n(\mathbf{k})$ of (Ga,Mn)As which are split by the exchange field h . The index n labels the two heavy-hole bands ($n=1, 2$), two light-hole bands ($n=3, 4$), both of the Γ_8 symmetry and total angular momentum $J=3/2$ in the Γ -point, and two split-off bands ($n=5, 6$) with the Γ_7 symmetry and $J=1/2$ in the Γ

point (see Chap. 3 of Ref. 27). Note that spin is not a good quantum number owing to the presence of SOI. Expectation value of spin along any of the Fermi surfaces can be visualized as a spin texture rather than having separate spin up and spin down bands. An example in Fig. 1(b) that corresponds³⁰ to the $n=1,2$ bands of Hamiltonian (2) with $\hbar \rightarrow 0$, shows that for each \mathbf{k} there are two states with opposite spin whose direction, however, depends on \mathbf{k} , contrary to systems without SOI.

B. Scattering on random Mn impurities

In order to get finite conductivity at zero temperature, we need to go beyond the virtual-crystal concept of Eq. (2). We follow Ref. 31 and use the Fermi golden rule (in first-order Born approximation treatment of V_{dis}) as the simplest model of scattering to calculate the transport scattering rates $\Gamma_{n,\mathbf{k}}$ of the Bloch states from Eq. (2),

$$\Gamma_{n,\mathbf{k}} = \frac{2\pi}{\hbar} N_{Mn} \times \sum_{n'} \int \frac{d^3k'}{(2\pi)^3} |M_{nn'}^{\mathbf{k}\mathbf{k}'}|^2 \delta[E_n(\mathbf{k}) - E_{n'}(\mathbf{k}')] \times (1 - \cos \theta_{vv'}), \quad (3)$$

where we use³¹ $\theta_{vv'}$, the angle subtended by the velocities $\mathbf{v}_n(\mathbf{k})$ and $\mathbf{v}_{n'}(\mathbf{k}')$ to take into account \mathbf{v} which need not be parallel to \mathbf{k} in case the combined effect of the SOI and magnetization distorts the Fermi surfaces as suggested by the sketch in Fig. 1(a).

Substitutional Mn act as acceptors and their magnetic moments participate in the ferromagnetic order of (Ga,Mn)As. Acknowledging the magnetic and nonmagnetic part of V_{dis} , we take

$$M_{nn'}^{\mathbf{k}\mathbf{k}'} = \langle z_{\mathbf{k}'n'} | M^B + M^C | z_{\mathbf{k}n} \rangle \quad (4)$$

for the scattering matrix elements between two eigenstates of the Hamiltonian (2). In the six-band notation of Eq. (2), the magnetic part of a single Mn impurity scattering operator is

$$M^B = J_{pd} S_{Mn} \hat{e}_M \cdot \mathbf{s}, \quad (5)$$

corresponding to the second term in Eq. (1). Explicit form of the spin 6×6 matrices \mathbf{s} is again given in the first of Ref. 26. The nonmagnetic part M^C describes screened Coulomb attraction of the valence holes to the ionized acceptors and we therefore take

$$M^C = V(|\mathbf{k} - \mathbf{k}'|) \mathbb{1}, \quad V(q) = -\frac{e^2}{\varepsilon} \frac{1}{q^2 + q_{TF}^2}, \quad (6)$$

where $\mathbb{1}$ denotes a 6×6 unity matrix, ε is the host semiconductor dielectric constant, $q_{TF} = \sqrt{e^2 g / \varepsilon}$ the Thomas-Fermi screening wavevector,^{21,32} and g the density of states at the Fermi level.

It is important that the two scattering operators (5) and (6) add up “coherently” in Eq. (4). If Eq. (3) contained the “incoherent” sum $|M_{nn'}^{\mathbf{k}\mathbf{k}'}|^2 = |\langle z_{\mathbf{k}'n'} | M^B | z_{\mathbf{k}n} \rangle|^2 + |\langle z_{\mathbf{k}'n'} | M^C | z_{\mathbf{k}n} \rangle|^2$ this would describe a physically different situation with two distinct types of scatterers, magnetic, and nonmagnetic ones. Such incoherent sum, with appropriately defined scattering

operators, was used earlier²¹ to describe more realistic (Ga,Mn)As systems that contain interstitial Mn atoms or As antisites in addition to the substitutional Mn.

To summarize our model description of substitutional Mn impurities in GaAs, the Mn atoms in $\text{Ga}_{1-x}\text{Mn}_x\text{As}$ enter our model at three different places: (i) As acceptors and in the absence of other dopants they determine the Fermi level E_F and therefore the density of states and Fermi velocities. (ii) On the virtual-crystal approximation (VCA) level, they cause the ferromagnetic-exchange splitting of the hole bands, and (iii) because of the random distribution in the lattice, the Mn impurities also cause scattering. The essential feature of the Mn impurity potentials for the AMR is that they contain components which are proportional to the Mn local moments and that these moments are ordered in the ferromagnetic state, as expressed in Eq. (5). We stress that considering (ii) and (iii) simultaneously leads to only a small “double-counting” error in the description of the effect of the Mn-related impurity potential. In terms of the VCA, we assume in (ii) that each site on the cation (Ga) sublattice of the host semiconductor is occupied by a mixture of x Mn and $1-x$ Ga. This yields an effective mean potential which shares the full periodicity of the host zinc-blende lattice. Strictly speaking, the scattering potential of randomly distributed Mn on the cation sublattice should be described as the difference between the full impurity potential due to Mn and the above VCA potential. Similarly the remaining sites occupied by Ga should be described by the difference between the Ga potential and the VCA potential. Ignoring the latter difference and taking the full Mn impurity potential for sites occupied by Mn when describing scattering in (iii) is therefore not a precise procedure but it introduces only a small error for Mn dopings not exceeding several percent.

C. Conductivity of (Ga,Mn)As in the relaxation-time approximation

We now calculate the conductivity tensor using the semiclassical formula based on the Boltzmann transport equation^{21,32}

$$\sigma_{ij} = e^2 \sum_n \int \frac{d^3k}{(2\pi)^3} (\hbar \Gamma_{n\mathbf{k}})^{-1} v_n^i(\mathbf{k}) v_n^j(\mathbf{k}) \delta[E_F - E(\mathbf{k})]. \quad (7)$$

We assume zero temperature hence the conductivity is determined exclusively by states on the Fermi level E_F . The Fermi velocities are calculated as $\mathbf{v}_n(\mathbf{k}) = (1/\hbar) \nabla_{\mathbf{k}} E_n$. In our model of one particular material, (Ga,Mn)As, the conductivity tensor depends on the direction of magnetization \hat{e}_M through Eqs. (2) and (5), that is owing to the combined effect of magnetization and SOI. More generally, we can divide (the models of) materials exhibiting the AMR into those in which $v_n^i(\mathbf{k})$ in Eq. (7) is magnetization dependent, as sketched in Fig. 1(a), and those which have a magnetization-dependent transport relaxation times $(\hbar \Gamma_{n\mathbf{k}})^{-1}$. Among the latter, we can still discriminate those where the magnetization-dependence enters through the scattering operator M [denoted $M^B + M^C$ in Eq. (4)] as sketched in Fig. 1(b) and those where the SOI- and magnetization-induced anisotropy of wave functions in Eq. (4) becomes important as it symbolizes Fig. 1(c).

Generally, the tensor (7) may be nondiagonal and the resistivity tensor ρ_{ij} is its inverse. Here we consider a “pure-AMR-configuration” where σ_{ij} is symmetric, i.e. free of any antisymmetric Hall components. It can be envisaged as a Hall-bar device fabricated from a thin (Ga,Mn)As film with an arbitrary in-plane magnetization. Experimentally, the magnetization will be controlled by a weak magnetic field whose direct effect on the AMR will be neglected. The longitudinal and transverse voltage drops are proportional to ρ_{xx} and ρ_{xy} ; spherical approximation (see Sec. II A) makes both the orientation of the film and of the Hall-bar device with respect to the crystallographic axes irrelevant. In an out-of-plane configuration, the resistivity acquires an antisymmetric anomalous Hall component, see Ref. 33 for a comprehensive review. For the in-plane configuration considered here, the resistivity is completely symmetric, $\rho_{xy}(-\hat{e}_M) = \rho_{xy}(\hat{e}_M) = \rho_{yx}(\hat{e}_M)$, and obeys $\rho_{xy}(\phi)/\rho_{av} = C_I \sin 2\phi$ where ϕ is the angle between magnetization and current (Hall-bar device) direction. This is a well-known result for isotropic systems with symmetry broken by the current flow, see for instance the derivation in Ref. 34. The diagonal resistivity, $\rho_{xx}(\phi) = \rho_{av}(1 + C_I \cos 2\phi)$, then carries the same information about AMR as $\rho_{xy}(\phi)$, which is concentrated into the noncrystalline AMR coefficient C_I [ρ_{av} is the angular average of $\rho_{xx}(\phi)$].

We use the following definition of the AMR

$$\text{AMR} \equiv -2 \frac{\sigma_{\parallel} - \sigma_{\perp}}{\sigma_{\parallel} + \sigma_{\perp}} = 2 \frac{\rho_{\parallel} - \rho_{\perp}}{\rho_{\parallel} + \rho_{\perp}}, \quad (8)$$

where σ_{\parallel} and σ_{\perp} (ρ_{\parallel} and ρ_{\perp}) are the longitudinal conductivities (resistivities) for current parallel and perpendicular to the magnetization, respectively. Note that the off-diagonal resistivities vanish for $\phi=0$ or 90° . For practical purposes, we can set \hat{e}_M in the x direction and $\sigma_{\parallel} \equiv \sigma_{xx}$, $\sigma_{\perp} \equiv \sigma_{yy}$ as long as we stay with the spherical approximation. The AMR of Eq. (8) equals to $2C_I$.

III. NONCRYSTALLINE AMR OF HEAVY HOLES IN THE SPHERICAL APPROXIMATION

In this Section, we first show that within our description of metallic (Ga,Mn)As samples, the AMR trends are governed by the mechanism sketched in Fig. 1(b). Then we proceed to showing that only heavy-hole bands need to be considered when analyzing the basic AMR characteristics in (Ga,Mn)As on a qualitative level.

A. Origins of anisotropy

Let us consider how the conductivity in Eq. (7) can become magnetization-dependent. In agreement with the intuitive analysis of Fig. 1, magnetization direction \hat{e}_M can enter Eq. (7) either via (a) the group velocity components v_n^i or (b,c) the scattering rates Γ_{nk} . Considering Eqs. (3) and (4), the scattering rates may depend on \hat{e}_M either through (b) the scattering operator ($M_B + M_C$ in our specific case) or (c) the wave functions $|z_{knl}\rangle$ and/or energies $E_n(\mathbf{k})$ and density of states of the carrier bands. The last mechanism, for example, lies at the heart of the s - d model of AMR in transition metals⁶ where isotropic and spin-independent scattering op-

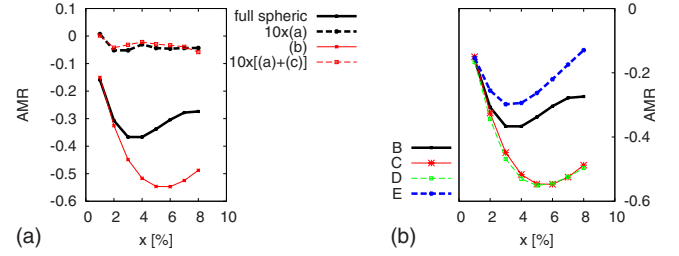


FIG. 2. (Color online) AMR as a function of Mn doping x in an idealized model of (Ga,Mn)As. Physical origin of the deep minimum is explained in the third paragraph after Eq. (21). *Left*: study of the influence of the three mechanisms (a,b,c) sketched in Fig. 1 on the total AMR. The model in spherical approximation as of Sec. II, serves as a reference (“full spheric”). Note that the upper two curves are upscaled by a factor of 10. *Right*: subsequent approximations (see text) aiming toward an analytically solvable model. Note that (B) and (C) is the same as full spheric and (b) on the left panel, respectively, while (D) and (E) correspond to gradual decoupling of the light holes.

erators have been assumed.^{19,20} The anisotropy arises due to the competition of SOI and magnetization which splits the five d states according to l_M , their angular momentum projection along \hat{e}_M . These states play the role of $|z_{k'n'}\rangle$ in Eq. (4), and because of their l_M -dependent spatial form they cause \hat{e}_M -dependent scattering rates Γ_{nk} in the s states that carry the current. Plugged back into Eq. (3), these anisotropic scattering rates may lead to different σ_{xx} for \hat{e}_M parallel and perpendicular to the x direction, i.e., $\sigma_{\parallel} \neq \sigma_{\perp}$.

In (Ga,Mn)As, we are going to take advantage of the tunability that the effective model outlined in Sec. II offers: we will switch the particular mechanisms (a,b,c) on and off to see how important they are for the total AMR. We use the band-structure model as described in Sec. II A (termed “full spherical”) as a reference. Within this full spherical model, the calculated AMR as a function of Mn doping x is negative in the considered range between 2% and 10% and its magnitude reaches a clear maximum as shown by the middle curve in the left panel of Fig. 2 (the maximum is related to the competition between the electric and magnetic parts of the scattering operator as we explain in Sec. IV). To see the effect of the mechanism (b) alone, we set $h=0$ in Eq. (2) but leave the scatterer anisotropy unchanged by keeping nonzero J_{pd} in Eq. (5). The bottom curve in the left panel of Fig. 2 demonstrates that the AMR quantitatively changes within a factor of 2 but its overall form remains the same.

On the other hand, the result alters dramatically when we switch off the anisotropy in the scattering operator [mechanism (b)] or the anisotropy in relaxation rates as a whole [mechanisms (b) and (c) together]. The former is accomplished by setting $M_B=0$ in Eq. (4), the latter is done by replacing Γ_{nk} by a constant whose value is irrelevant because it cancels out in Eq. (8). In both cases, we obtain AMR that is more than an order of magnitude smaller than for the full spherical model, see Fig. 2. Herewith we find that contrary to metals,^{3,4} the $\Gamma_{n,\mathbf{k}}=\text{const.}$ approximation fails to account for AMR in (Ga,Mn)As or, in other words, the AMR mechanism of Fig. 1(a) does not play a significant role in (Ga,Mn)As. Given the small difference between the curves

labelled (a) and (a)+(c) on the left panel of Fig. 2, we conclude that the mechanism of Fig. 1(c) *alone* cannot account for the AMR in this material either. In summary, our results indicate that while mechanism (b) is a crucial part of the AMR model of metallic (Ga,Mn)As, the other mechanisms (a,c) provide only quantitative corrections and when left alone without mechanism (b), they produce negligible AMR.

B. Heavy holes

The next simplification of the model we make in order to provide a simple physical picture of the AMR in (Ga,Mn)As, is to neglect the light holes. We can accomplish this in two steps: we first discard the current carried by the light holes, i.e., sum in Eq. (7) over $n=1,2$ only, and then also disable the scattering from the heavy-hole to light-hole bands, i.e. sum in Eq. (3) over $n'=1,2$ only. Numerical calculation again shows that this procedure does not alter the qualitative behavior of the AMR. All levels of approximations are summarized in the right panel of Fig. 2. For completeness, we start with the “full spheric” reference (curve labeled by “B”) as on the left panel and proceed to suppressing the band polarization by putting $h=0$ in Eq. (2) which yields the curve “C.” Omission of light-holes from current-carrying states in the transport equation but not from the final states in the scattering matrix elements produces the data labeled by “D,” and the completely heavy-hole-only model (six-band model where the other four bands are disregarded) is denoted by “E.”

For further studies of this model it may be interesting that the difference between curves C and D is remarkably small, in other words, the anisotropy of the light-hole transport is almost identical to that of the heavy holes, provided we have set $h=0$ in Eq. (2). However, the main conclusion of this section is that, within the studied range of Mn doping, the AMR is determined by the anisotropy of the relaxation rates of heavy holes induced by the Mn electromagnetic scatterers. This allows us to derive an approximate analytical formula for the AMR in (Ga,Mn)As which we discuss in the following section.

IV. QUALITATIVE ANALYTICAL RESULTS FOR AMR IN (Ga,Mn)As

We first provide analytical expressions for the AMR corresponding to the curve “E” in Fig. 2 with an additional approximation that the current \mathbf{I} is proportional only to the transport lifetime of carriers with $\mathbf{v}_n \parallel \mathbf{I}$. Using the explicit form of the heavy-hole wave functions given in Ref. 30, the transport scattering rates of Eq. (3) corresponding to $M^B + M^C$ of Eqs. (5) and (6) can be evaluated as

$$\Gamma_{\pm}(0) = \frac{\pi}{2} \left[\frac{a^2}{k_F^2} \left(12 + 18b + \frac{8}{b-1} - (1+3b)^2 \ln \frac{b+1}{b-1} \right) + 2k_F^2 \mp a \left(4 + 6b + 6b^2 - (b+1)(1+3b)^2 \ln \frac{b+1}{b-1} \right) \right], \quad (9)$$

where $\Gamma_{\pm}(\phi)$ are the scattering rates of the two heavy-hole

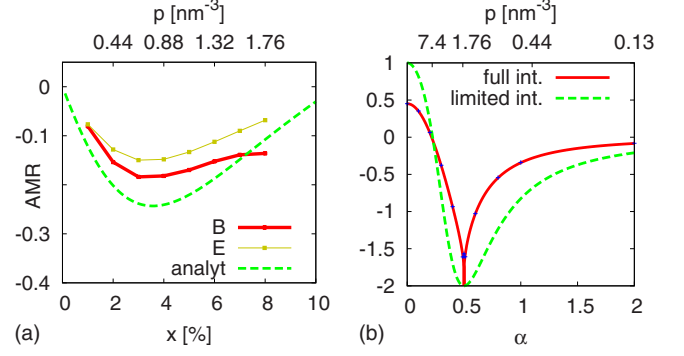


FIG. 3. (Color online) (a) The analytical model of AMR based on Eqs. (9) and (10). Curves B and E are taken from the right panel of Fig. 2. Estimates of the hole concentrations shown on the upper axis assume one hole per Mn and neglect the light-hole bands. (b) The AMR as a function of the effective Coulomb scattering strength given by Eq. (19). The “limited-integration” model (only states with \mathbf{k} parallel to the current) is represented by Eq. (18), the integrated model where all states contribute to the current is described after Eq. (20).

bands with ϕ denoting the angle between \mathbf{k} and \hat{e}_M . Next, we get

$$\Gamma_{\pm} \left(\frac{1}{2} \pi \right) = \frac{\pi}{2} \left[\frac{1}{3} k_F^2 + \frac{a^2}{k_F^2} \left(12 + 18b + \frac{8}{b-1} - (1+3b)^2 \ln \frac{b+1}{b-1} \right) \right]. \quad (10)$$

We used short hands $a = -(e^2/2\epsilon k_F^2)/J_{pd} S_{Mn}$ with k_F denoting the common Fermi wave vector of the heavy holes, and $b = -(1+q_{TF}^2/k_F^2)$.

Conductivities are evaluated as

$$\sigma_{\parallel} \propto \frac{1}{\Gamma_{+}(0)} + \frac{1}{\Gamma_{-}(0)}, \quad (11)$$

$$\sigma_{\perp} \propto \frac{1}{\Gamma_{+} \left(\frac{1}{2} \pi \right)} + \frac{1}{\Gamma_{-} \left(\frac{1}{2} \pi \right)} = \frac{2}{\Gamma_{+} \left(\frac{1}{2} \pi \right)}, \quad (12)$$

and yield AMR which is up to an overall factor of ≈ 2 the same as if we performed the complete \mathbf{k} -integration in Eq. (7), see Fig. 3(a). The approximation of taking into account only states with $\mathbf{k} \parallel \mathbf{I}$ is therefore qualitatively valid.

Short-range scatterers

Results of Eqs. (9) and (10) are analytical but the formula for AMR is rather complicated. We can attain a clear insight into how the observed AMR trends arise if we further simplify the model. We replace $M^B + M^C$ of Eqs. (5) and (6) by another scattering operator

$$M^{s.r.} \propto \hat{e}_M \cdot \mathbf{s} + \alpha \mathbf{1}. \quad (13)$$

That is, we assume \mathbf{k} -independent electric part of the scattering potential.

The transport scattering rates of Eq. (3) again depend only on the angle ϕ ,

$$\Gamma_{\pm}(\phi) \propto \frac{1}{6} \cos^2 \phi \pm \alpha \cos \phi + \alpha^2 + \frac{1}{12}, \quad (14)$$

and specifically for states with \mathbf{k} parallel and perpendicular to \hat{e}_M , we get

$$\Gamma_{\pm}(0) \propto \left(\alpha \pm \frac{1}{2}\right)^2, \quad \Gamma_{\pm}\left(\frac{1}{2}\pi\right) \propto \alpha^2 + \frac{1}{12}. \quad (15)$$

Conductivities evaluated using Eqs. (11) and (12) simplify to

$$\sigma_{\parallel} \propto \frac{1}{\left(\alpha + \frac{1}{2}\right)^2} + \frac{1}{\left(\alpha - \frac{1}{2}\right)^2} \quad (16)$$

$$\sigma_{\perp} \propto \frac{2}{\Gamma_{+}\left(\frac{1}{2}\pi\right)} = \frac{2}{\alpha^2 + \frac{1}{12}}, \quad (17)$$

which gives, using Eq. (8), our previous result^{8,30}

$$\text{AMR} = -\frac{20\alpha^2 - 1}{24\alpha^4 - 2\alpha^2 + 1}. \quad (18)$$

In order to link this result, plotted in Fig. 3(b), to the previous one that is based on the full form of the Coulomb scattering operator given by Eq. (6), we need to focus on the parameter α . It represents the effective strength of the electric part relative to the magnetic part of the scattering potential of the Mn ions. We can estimate α as an average over the Fermi surface of the more realistic $V(|\mathbf{k}-\mathbf{k}'|)$ from Eq. (6),

$$\alpha = \frac{\langle V \rangle_{FS}}{J_{pd} S_{Mn}} = \frac{e^2/\varepsilon}{J_{pd} S_{Mn}} \cdot \frac{1}{4k_F^2} \ln\left(1 + \frac{4k_F^2}{q_{TF}^2}\right). \quad (19)$$

Explicitly, $\langle V \rangle_{FS} \equiv (4\pi k_F^2)^{-1} \int_{FS} d^2k' V(|\mathbf{k}-\mathbf{k}'|)$ with \mathbf{k} fixed to an arbitrary Fermi wave vector, $|\mathbf{k}|=k_F$. The integral is taken over the Fermi surface.

We thus find that the relative strength of the Coulomb scattering increases with decreasing hole density, $p \approx k_F^3/(3\pi^2)$, due to the screened long-range nature of the Coulomb interaction which contrasts the short-range of the magnetic scattering. Namely, the momentum transfers q scale down with k_F and we increasingly get to feel the singularity of $V(q)$ at $q=0$ even though it is rounded by the screening, see Eq. (6). Assuming a value $p=0.5 \text{ nm}^{-3}$ which is realistic in (Ga,Mn)As, we have $k_F \approx 2.5 \text{ nm}^{-1}$, $q_{TF} \approx 1.6 \text{ nm}^{-1}$, and $\alpha \approx 1.0$.

Equation (19) provides the link between α and p which is determined by x , i.e. between horizontal axes of Figs. 3(a) and 3(b). Qualitatively, increasing x and thus also increasing k_F implies decreasing α because the scattering rate due to the magnetic part scales $\propto k_F^2$ while the scattering rate due to the Coulomb scattering given by M^C of Eq. (6) grows considerably slower. If we estimate $V(|\mathbf{k}-\mathbf{k}'|)$ by $V(2k_F)$, the growth will be only $\propto k_F^2/(k_F^2 a^2 + k_F a/\pi)$ where $a \approx 1.4 \text{ nm}$ is the effective Bohr radius in GaAs. Behavior of the more sophisticated estimate used in Eq. (19) is qualitatively the same.

The simple form of scattering rates in Eq. (14) allows to analytically perform the full integration over \mathbf{k} in Eq. (7) and to obtain more precise results for conductivity. For $\sigma_{\parallel} = \sigma_{\parallel}^+ + \sigma_{\parallel}^-$ we get

$$\sigma_{\parallel}^{\pm} \propto \int_{FS} \frac{d^2k \cos^2 \phi}{\Gamma_{\pm}(\phi)}. \quad (20)$$

The proportionality factor is e^2 times squared Fermi velocity times the density of states at the Fermi level. Conductivities of the two bands are equal, so that

$$\sigma_{\parallel} \propto 12 - 36\alpha \ln \left| \frac{\alpha + \frac{1}{2}}{\alpha - \frac{1}{2}} \right| + \sqrt{18} \frac{24\alpha^2 - 1}{\sqrt{|6\alpha^2 - 1|}} \operatorname{arcsinh} \frac{\sqrt{|6\alpha^2 - 1|/18}}{\left| \alpha^2 - \frac{1}{4} \right|}, \quad \alpha^2 > \frac{1}{6}, \quad (21)$$

and the same result with $\operatorname{arcsinh}$ replaced by arcsin applies for $\alpha^2 < \frac{1}{6}$.

In order to evaluate σ_{\perp} , we employ a straightforward identity $\sigma_{\parallel}^{\pm} + 2\sigma_{\perp}^{\pm} = T^{\pm}$ with

$$T^{\pm} = \frac{2\sqrt{18}}{\sqrt{|6\alpha^2 - 1|}} \operatorname{arcsinh} \frac{\sqrt{|6\alpha^2 - 1|/18}}{\left| \alpha^2 - \frac{1}{4} \right|}, \quad \alpha^2 > \frac{1}{6},$$

and again with arcsin for $\alpha^2 < \frac{1}{6}$, which can be derived by inserting $\cos^2 \phi = 1 - \sin^2 \phi$ into Eq. (20). The AMR evaluated using Eq. (8) is shown as the solid curve in Fig. 3(b).

Both models with simplified scattering operator $M^{s,r}$ exhibit qualitatively the same behavior of AMR as a function of α : positive AMR for α close to zero, sign change to negative AMR already for a small value of α , maximum AMR magnitude at $\alpha=1/2$, and vanishing AMR for $\alpha \rightarrow \infty$. A comparison between Figs. 3(a) and 3(b) reveals that the outstanding feature of the AMR at $|\alpha|=1/2$ makes its way³⁵ up to the full spherical model where it becomes broadened to the wide maximum (around $x \approx 4\%$ in Fig. 2). Based on the model that employs $M^{s,r}$ of Eq. (13), we now analyze the origin of the very large negative AMR at $|\alpha|=1/2$.

This maximum $|\text{AMR}|$ value, seen also in the more elaborate models of Fig. 2, follows from the diverging conductivity σ_{\parallel} given by Eqs. (16) or (21) which is caused by vanishing scattering rate $\Gamma_{\mp}(0)$ for $\alpha = \pm 1/2$. The scattering matrix element in Eq. (4) vanishes for any n', \mathbf{k}' , and so does the integral (7), when $|z_{\mathbf{k}n}\rangle$ is an eigenstate to $M^{s,r}$ with eigenvalue zero; for illustrative purposes, consider $M^{s,r} = s_x + \alpha$, i.e., \hat{e}_M pointing to the right in terms of Fig. 1. The absence of scattering occurs in the $-$ band [radial-inward spin texture in Fig. 1(b)] for $\alpha=1/2$ when \mathbf{k} is parallel to the x direction; the kind reader who prefers an explicit calculation to sketches is referred to Ref. 30. Such infinite conductivity will of course not occur in realistic systems; as soon as the dependences on momentum transfer of the electric and mag-

netic parts of the scattering potential will not be exactly the same, the eigenstate property of $|z_{kn}\rangle$ is lost. This is the case when we replace $M^{s.r.}$ by the original $M^B + M^C$ of Eqs. (5) and (6). However, as Fig. 3(a) shows, there still remains a maximum in σ_{\parallel} which translates into a maximum of $|\text{AMR}|$ as a fingerprint of the original σ_{\parallel} singularity.

Positive AMR for purely magnetic scattering ($\alpha=0$) that follows from Eq. (18) can also be understood using the basic properties of spin-3/2 states.¹¹ The idea is that $|z_{kn}\rangle$ is an eigenstate (with nonzero eigenvalue) to $\hat{e}_M \cdot \mathbf{s}$ for \mathbf{k} oriented along \hat{e}_M thereby allowing scattering to a state with $-\mathbf{k}$ that contributes strongly to the transport relaxation rate of Eq. (3). On the other hand, matrix elements of $\hat{e}_M \cdot \mathbf{s}$ vanish³⁰ between states with $\mathbf{k}, \mathbf{k}' \perp \hat{e}_M$; scattering and resistivity are therefore suppressed for the magnetization perpendicular to the current (see also illustrative sketch in Fig. 4 of Ref. 11). Relation $\sigma_{\perp} > \sigma_{\parallel}$ ($\text{AMR} > 0$) for $\alpha=0$, obtained from this simplified analysis of the leading scattering channels which contribute to transport, is confirmed by calculations that even take into account all final states \mathbf{k}' for the scattering and include the integration over all \mathbf{k} -states in Eq. (7). The sign of the AMR changes quickly from positive to negative on adding the electric component of the scattering potential. In the model of short range potentials, summarized by Eq. (18), it occurs at $\alpha=1/\sqrt{20}$. Recall that for realistic impurities with screened long-range Coulomb potential the transition can be triggered by changing hole density, as explained in the discussion of Fig. 2.

At the end of this section, let us make several remarks to the experimental relevance of the present work. Our central thesis is that the sign and magnitude of the AMR in (Ga,Mn)As and related materials can be tuned by α , i.e., the character of the electromagnetic scatterers in the material. This thesis, and the discussion presented are limited by several factors: (i) the systems in question must be sufficiently metallic so that the kinetic-exchange effective-Hamiltonian approach outlined in Sec. II A is justified, (ii) only substitutional Mn should be present, in order to keep the relatively simple scattering description of Sec. II B applicable, (iii) the anisotropic scatterer mechanism [see Fig. 1(b)] must dominate, paving the way for the simplifications of Sec. III and IV, (iv) the noncrystalline AMR must dominate for the spherical approximation to have any predictive power, and (v) the error of the RTA used in Sec. II B must not be severe. Restricting our discussion to systems complying with (i), III-V materials with less anisotropic Fermi surfaces such as (In,Mn)As or (In,Mn)Sb seem promising. Although the point (ii) is not a major obstacle to the model building and other sources of scattering such as interstitial Mn can be taken into account,²¹ optimally annealed samples would be preferable. In any new material, the validity of (iii) should be verified anew using the experimentally relevant parameters.

Regarding the RTA, we expect (iv) and (v) to be closely related. It has been shown in Ref. 22 that the RTA does not provide the exact solution of the Boltzmann equation. Even in the simple case of a spherical model in (Ga,Mn)As whose isotropy is however broken by the magnetization, we should solve an integral equation rather than merely evaluate inte-

grals as in Eq. (3). Whenever significant crystalline AMR components occur in systems with highly nonspherical Fermi surfaces, the error of the RTA may get out of hand. Nonetheless, the main AMR features shown in Fig. 3(b) are common both to the RTA and to the exact solution of Boltzmann equation: the minimum at $\alpha=1/2$ (see also Fig. 2) follows from the annihilative property of the scattering operator and the positive AMR at $\alpha=0$ was verified on the most simplified model using the exact solution of Boltzmann equation.¹¹

V. SUMMARY

Noncrystalline anisotropic magnetoresistance (AMR) is governed only by the angle between magnetization and current rather than by their orientation with respect to crystallographic axes, as opposed to the crystalline AMR. The physical origin of the AMR is the combination of spin-orbit interaction (SOI) and of the broken symmetry due to the presence of magnetization. More specifically, three distinct mechanisms may lead to the noncrystalline AMR: Fermi surfaces distorted from the spherical shape that imply anisotropic Fermi velocities, and anisotropic scattering rates, either due to anisotropic wave functions or due to the anisotropic scatterers. We note that the *s-d* model which is sometimes invoked to qualitatively explain the AMR in ferromagnetic transition metals, is a variation of the anisotropic wave function mechanism. Because of the competing effect of the SOI and magnetization (which are both present only in the low-mobility *d* states) one may expect weak AMR.

On the other hand, we have shown that (Ga,Mn)As constitutes a textbook example of a system where strong AMR can be expected since the two agents are mostly separated: polarized Mn ions act as anisotropic scatterers while the current-carrying valence-band states bring in the SOI. Quantitatively, the latter are also partly polarized but we have demonstrated that for the typical experimental range of Mn dopings in metallic (Ga,Mn)As samples ($x=2 \sim 10\%$), the anisotropic scatterer mechanism is dominant. A simple model which neglects the other two mechanisms provides analytical results which predict the correct sign of the AMR (resistivity parallel to magnetization is smaller than perpendicular to magnetization) and identify its origin—destructive interference between electric and magnetic part of the scattering potential (of ionized Mn acceptors) for carriers moving parallel to magnetization.

ACKNOWLEDGMENTS

We gratefully acknowledge Jan Mašek for his advice regarding the range of validity of the model in Sec. II A, Jan Zemen for his assistance in numerical modeling, and the following host of research-supporting governmental instruments: Grants No. AV0Z10100521, No. LC510, No. KAN400100652, and No. FON/06/E002 of GA ČR, and Grant No. KJB100100802 of GA AV of the Czech republic, the NAMASTE (FP7 Grant No. 214499) and SemiSpinNet projects (FP7 Grant No. 215368), SWAN-NRI, ONR under Grant No. onr-n000140610122, NSF under Grant No. DMR-0547875, and also Præmium Academiæ.

- ¹W. Thomson, Proc. R. Soc. Lond. **8**, 546 (1857).
- ²C. Chappert, A. Fert, and F. N. V. Dau, Nature Mater. **6**, 813 (2007).
- ³J. Banhart and H. Ebert, Europhys. Lett. **32**, 517 (1995).
- ⁴H. Ebert, A. Vernes, and J. Banhart, Solid State Commun. **113**, 103 (1999).
- ⁵N. F. Mott, Adv. Phys. **13**, 325 (1964).
- ⁶A. P. Malozemoff, Phys. Rev. B **34**, 1853 (1986).
- ⁷T. Jungwirth, J. Sinova, J. Mašek, J. Kučera, and A. H. MacDonald, Rev. Mod. Phys. **78**, 809 (2006).
- ⁸A. W. Rushforth, K. Výborný, C. S. King, K. W. Edmonds, R. P. Champion, C. T. Foxon, J. Wunderlich, A. C. Irvine, P. Vašek, V. Novák, K. Olejník, J. Sinova, T. Jungwirth, and B. L. Gallagher, Phys. Rev. Lett. **99**, 147207 (2007).
- ⁹W. Limmer, J. Daeubler, L. Dreher, M. Glunk, W. Schoch, S. Schwaiger, and R. Sauer, Phys. Rev. B **77**, 205210 (2008) and references therein to the experimental work on AMR in general.
- ¹⁰Thus induced anisotropy of Fermi surfaces can nicely be illustrated on Fig. 1. Consider the spin texture in Fig. 1(b) as a typical example of SOI effect. Exchange splitting due to magnetization oriented horizontally in Fig. 1, effectively acts as a Zeeman energy due to fictitious 'magnetic field' \mathbf{B} with the same orientation, see Eq. (2). The states with wave vector $\mathbf{k} \parallel \mathbf{B}$ will be shifted upward (downward) in energy because their spin is parallel (antiparallel) to \mathbf{B} while the states $\mathbf{k} \perp \mathbf{B}$ remain intact. This \mathbf{k} -anisotropic shift in energy can be translated into the splitting of Fermi wave vectors of the two originally degenerate bands.
- ¹¹M. Trushin, K. Výborný, P. Moraczewski, A. A. Kovalev, J. Schliemann, and T. Jungwirth, Phys. Rev. B **80**, 134405 (2009).
- ¹²W. Limmer, M. Glunk, J. Daeubler, T. Hummel, W. Schoch, R. Sauer, C. Bihler, H. Huebl, M. S. Brandt, and S. T. B. Goennenwein, Phys. Rev. B **74**, 205205 (2006).
- ¹³J. Wang, C. Sun, J. Kono, A. Oiwa, H. Munekata, L. Cywiński, and L. J. Sham, Phys. Rev. Lett. **95**, 167401 (2005).
- ¹⁴S. T. B. Goennenwein, S. Russo, A. F. Morpurgo, T. M. Klapwijk, W. Van Roy, and J. De Boeck, Phys. Rev. B **71**, 193306 (2005).
- ¹⁵F. Matsukura, M. Sawicki, T. Dietl, D. Chiba, and H. Ohno, Physica E **21**, 1032 (2004).
- ¹⁶H. X. Tang, R. K. Kawakami, D. D. Awschalom, and M. L. Roukes, Phys. Rev. Lett. **90**, 107201 (2003).
- ¹⁷T. Jungwirth, J. Sinova, K. Y. Wang, K. W. Edmonds, R. P. Champion, B. L. Gallagher, C. T. Foxon, Q. Niu, and A. H. MacDonald, Appl. Phys. Lett. **83**, 320 (2003).
- ¹⁸D. V. Baxter, D. Ruzmetov, J. Scherschligt, Y. Sasaki, X. Liu, J. K. Furdyna, and C. H. Mielke, Phys. Rev. B **65**, 212407 (2002).
- ¹⁹O. Jaoul, I. A. Campbell, and A. Fert, J. Magn. Magn. Mater. **5**, 23 (1977).
- ²⁰T. McGuire and R. Potter, IEEE Trans. Magn. **11**, 1018 (1975).
- ²¹T. Jungwirth, M. Abolfath, J. Sinova, J. Kučera, and A. H. MacDonald, Appl. Phys. Lett. **81**, 4029 (2002).
- ²²K. Výborný, A. A. Kovalev, J. Sinova, and T. Jungwirth, Phys. Rev. B **79**, 045427 (2009).
- ²³T. Jungwirth, J. Sinova, A. H. MacDonald, B. L. Gallagher, V. Novák, K. W. Edmonds, A. W. Rushforth, R. P. Champion, C. T. Foxon, L. Eaves, E. Olejník, J. Mašek, S.-R. Eric Yang, J. Wunderlich, C. Gould, L. W. Molenkamp, T. Dietl, and H. Ohno, Phys. Rev. B **76**, 125206 (2007).
- ²⁴J. R. Schrieffer and P. A. Wolff, Phys. Rev. **149**, 491 (1966).
- ²⁵J. M. Luttinger, Phys. Rev. **102**, 1030 (1956); A. Baldereschi and N. O. Lipari, Phys. Rev. B **8**, 2697 (1973).
- ²⁶M. Abolfath, T. Jungwirth, J. Brum, and A. H. MacDonald, Phys. Rev. B **63**, 054418 (2001); T. Dietl, H. Ohno, and F. Matsukura, *ibid.* **63**, 195205 (2001).
- ²⁷R. Winkler, *Spin-Orbit Coupling Effects in Two-Dimensional Electron and Hole Systems* (Springer-Verlag, New York, 2003).
- ²⁸J. Okabayashi, A. Kimura, O. Rader, T. Mizokawa, A. Fujimori, T. Hayashi, and M. Tanaka, Phys. Rev. B **58**, R4211 (1998).
- ²⁹T. Jungwirth, K. Y. Wang, J. Mašek, K. W. Edmonds, J. König, J. Sinova, M. Polini, N. A. Goncharuk, A. H. MacDonald, M. Sawicki *et al.*, Phys. Rev. B **72**, 165204 (2005).
- ³⁰A. W. Rushforth, K. Výborný, C. S. King, K. W. Edmonds, R. P. Champion, C. T. Foxon, J. Wunderlich, A. C. Irvine, V. Novák, K. Olejník, A. A. Kovalev, J. Sinovae, T. Jungwirth, and B. L. Gallagher, J. Magn. Magn. Mater. **321**, 1001 (2009).
- ³¹J. M. Ziman, Phys. Rev. **121**, 1320 (1961).
- ³²N. W. Ashcroft and N. D. Mermin, *Solid State Physics* (Saunders College Publishing, Philadelphia, 1976).
- ³³N. A. Sinitsyn, J. Phys.: Condens. Matter **20**, 023201 (2008).
- ³⁴E. de Ranieri, A. W. Rushforth, K. Výborný, U. Rana, E. Ahmad, R. P. Champion, C. T. Foxon, B. L. Gallagher, A. C. Irvine, J. Wunderlich, and T. Jungwirth, New J. Phys. **10**, 065003 (2008).
- ³⁵Note that once we have set $\hbar=0$ in Eq. (2), the theoretical AMR depends on the Mn doping x only through the carrier density $p[\text{nm}^{-3}]=0.22 \times x[\%]$, because N_{Mn} appearing in Eq. (3) drops out in Eq. (8). This fact should not be taken *ad absurdum* ($N_{\text{Mn}} \rightarrow 0$) because we still assume that the substitutional Mn impurities provide the dominant source of scattering. Presence of other concurrent types of impurities [which is important when we compare the calculated AMR to experiments (Ref. 21)] will make the AMR depend on the ratio between their concentration and N_{Mn} . Nevertheless, this interplay will not simply obey Matthiessen's rule since we deal with anisotropic systems (Ref. 36).
- ³⁶J. S. Dugdale and Z. S. Basinski, Phys. Rev. **157**, 552 (1967).